



# Merging Gas-rich Galaxies That Harbor Low-luminosity Twin Quasars at $z = 6.05$ : A Promising Progenitor of the Most Luminous Quasars

Takuma Izumi<sup>1,2,3</sup> , Yoshiki Matsuoka<sup>4</sup> , Masafusa Onoue<sup>5,6,7,25</sup> , Michael A. Strauss<sup>8</sup> , Hideki Umehata<sup>9,10,11</sup> , John D. Silverman<sup>5,6,12,13</sup> , Tohru Nagao<sup>3,4</sup> , Masatoshi Imanishi<sup>1,2</sup> , Kotaro Kohno<sup>14,15</sup> , Yoshiki Toba<sup>1,4,16</sup> , Kazushi Iwasawa<sup>17,18</sup> , Kouichiro Nakanishi<sup>1,2</sup> , Mahoshi Sawamura<sup>1,12</sup> , Seiji Fujimoto<sup>19,20,21</sup> , Satoshi Kikuta<sup>12</sup> , Toshihiro Kawaguchi<sup>22</sup> , Kentaro Aoki<sup>23</sup> , and Tomotsugu Goto<sup>24</sup>

<sup>1</sup> National Astronomical Observatory of Japan, 2-21-1 Osawa, Mitaka, Tokyo 181-8588, Japan; [takuma.izumi@nao.ac.jp](mailto:takuma.izumi@nao.ac.jp)

<sup>2</sup> Department of Astronomical Science, The Graduate University for Advanced Studies, SOKENDAI, 2-21-1 Osawa, Mitaka, Tokyo 181-8588, Japan

<sup>3</sup> Amanogawa Galaxy Astronomy Research Center, Kagoshima University, 1-21-35 Korimoto, Kagoshima 890-0065, Japan

<sup>4</sup> Research Center for Space and Cosmic Evolution, Ehime University, 2-5 Bunkyo-cho, Matsuyama, Ehime 790-8577, Japan

<sup>5</sup> Kavli Institute for the Physics and Mathematics of the Universe (Kavli IPMU, WPI), The University of Tokyo Institutes for Advanced Study, The University of Tokyo, Kashiwa, Chiba 277-8583, Japan

<sup>6</sup> Center for Data-Driven Discovery, Kavli IPMU (WPI), UTIAS, The University of Tokyo, Kashiwa, Chiba 277-8583, Japan

<sup>7</sup> Kavli Institute for Astronomy and Astrophysics, Peking University, Beijing 100871, People's Republic of China

<sup>8</sup> Princeton University Observatory, Peyton Hall, Princeton, NJ 08544, USA

<sup>9</sup> Institute for Advanced Research, Nagoya University, Furocho, Chikusa, Nagoya 464-8602, Japan

<sup>10</sup> Department of Physics, Graduate School of Science, Nagoya University, Furocho, Chikusa, Nagoya 464-8602, Japan

<sup>11</sup> Cahill Center for Astronomy and Astrophysics, California Institute of Technology, 1200 E California Blvd., MC 249-17, Pasadena, CA 91125, USA

<sup>12</sup> Department of Astronomy, School of Science, The University of Tokyo, 7-3-1 Hongo, Bunkyo, Tokyo 113-0033, Japan

<sup>13</sup> Center for Astrophysical Sciences, Department of Physics & Astronomy, Johns Hopkins University, Baltimore, MD 21218, USA

<sup>14</sup> Institute of Astronomy, Graduate School of Science, The University of Tokyo, 2-21-1 Osawa, Mitaka, Tokyo 181-0015, Japan

<sup>15</sup> Research Center for the Early Universe, Graduate School of Science, The University of Tokyo, 7-3-1 Hongo, Bunkyo-ku, Tokyo 113-0033, Japan

<sup>16</sup> Academia Sinica Institute of Astronomy and Astrophysics, 11F of Astronomy-Mathematics Building, AS/NTU, No. 1, Section 4, Roosevelt Rd., Taipei 10617, Taiwan

<sup>17</sup> Institut de Ciències del Cosmos (ICCUB), Universitat de Barcelona (IEEC-UB), Martí i Franquès, 1, 08028 Barcelona, Spain

<sup>18</sup> ICREA, Pg. Lluís Companys 23, 08010 Barcelona, Spain

<sup>19</sup> Department of Astronomy, The University of Texas at Austin, Austin, TX 78712, USA

<sup>20</sup> Cosmic Dawn Center (DAWN), Copenhagen, Denmark

<sup>21</sup> Niels Bohr Institute, University of Copenhagen, Jagtvej 128, 2200 Copenhagen N, Denmark

<sup>22</sup> Department of Economics, Management and Information Science, Onomichi City University, Hisayamada 1600-2, Onomichi, Hiroshima 722-8506, Japan

<sup>23</sup> Subaru Telescope, National Astronomical Observatory of Japan, Japan

<sup>24</sup> Institute of Astronomy, National Tsing Hua University, No. 101, Section 2, Kuang-Fu Rd., Hsinchu 30013, Taiwan

Received 2024 April 26; revised 2024 June 7; accepted 2024 June 11; published 2024 August 29

## Abstract

We present Atacama Large Millimeter/submillimeter Array [C II] 158  $\mu\text{m}$  line and underlying far-IR continuum emission observations ( $0''.57 \times 0''.46$  resolution) toward a quasar–quasar pair system recently discovered at  $z = 6.05$ . The quasar nuclei (C1 and C2) are faint ( $M_{1450} \gtrsim -23$  mag), but we detect very bright [C II] emission bridging the 12 kpc between the two objects and extending beyond them (total luminosity  $L_{[\text{C II}]} \simeq 6 \times 10^9 L_{\odot}$ ). The [C II]-based total star formation rate of the system is  $\sim 550 M_{\odot} \text{yr}^{-1}$  (the IR-based dust-obscured star formation is  $\sim 100 M_{\odot} \text{yr}^{-1}$ ), with a [C II]-based total gas mass of  $\sim 10^{11} M_{\odot}$ . The dynamical masses of the two galaxies are large ( $\sim 9 \times 10^{10} M_{\odot}$  for C1 and  $\sim 5 \times 10^{10} M_{\odot}$  for C2). There is a smooth velocity gradient in [C II], indicating that these quasars are a tidally interacting system. We identified a dynamically distinct, fast-[C II] component around C1: detailed inspection of the line spectrum there reveals the presence of a broad-wing component, which we interpret as the indication of fast outflows with a velocity of  $\sim 600 \text{ km s}^{-1}$ . The expected mass-loading factor of the outflows, after accounting for multiphase gas, is  $\gtrsim 2 - 3$ , which is intermediate between AGN-driven and starburst-driven outflows. Hydrodynamic simulations in the literature predict that this pair will evolve to a luminous ( $M_{1450} \lesssim -26$  mag), starbursting ( $\gtrsim 1000 M_{\odot} \text{yr}^{-1}$ ) quasar after coalescence, one of the most extreme populations in the early Universe.

*Unified Astronomy Thesaurus concepts:* [Galaxy evolution \(594\)](#); [Quasars \(1319\)](#); [Galaxy mergers \(608\)](#); [Galaxy interactions \(600\)](#)

## 1. Introduction

In the hierarchical structure formation scenario, galaxies undergo multiple mergers over cosmic time. Models show that mergers of gas-rich galaxies trigger intense star formation and

fueling onto the central supermassive black holes (SMBHs), which appear as luminous quasars (e.g., Sanders et al. 1988; Di Matteo et al. 2005; Hopkins et al. 2006). Some theoretical models predict that subsequent feedback from the quasars, or active galactic nuclei (AGNs), plays a crucial role in driving the coevolution of SMBHs and host galaxies (King & Pounds 2015; Veilleux et al. 2020), leading to the observed tight correlation between the masses of SMBHs ( $M_{\text{BH}}$ ) and those of the host galaxy bulges observed in the local Universe (Kormendy & Ho 2013). Detections of galaxy-scale AGN-driven outflows in multiphase gas (e.g., Nesvadba et al. 2008;

<sup>25</sup> Kavli Astrophysics Fellow.

Aalto et al. 2012; Cicone et al. 2014), a higher AGN fraction in interacting/merging systems (e.g., Silverman et al. 2011; Goulding et al. 2018; Koss et al. 2018), and the global similarity in star formation and SMBH accretion histories over cosmic time (Madau & Dickinson 2014) support this scenario.

It is intriguing in this context that massive ( $\sim 10^{11} M_{\odot}$ ), quiescent, and old galaxies are already formed at  $z \sim 4 - 5$  (e.g., Carnall et al. 2023; Valentino et al. 2023), suggesting that a phase of rapid growth of galaxies and SMBHs, and their associated feedback, had happened at even higher redshifts. Indeed, more than 400 quasars with rest-UV magnitude of  $M_{1450} < -22$  mag are known at  $z > 5.7$  to date (Inayoshi et al. 2020; Fan et al. 2023), most of which have been identified by wide-field optical and near-IR surveys (e.g., Bañados et al. 2016; Jiang et al. 2016; Matsuoka et al. 2016, 2018a, 2018b). Sub/millimeter observations of the rest-frame far-IR (FIR) continuum and  $C^+ \ ^2P_{3/2} \rightarrow \ ^2P_{1/2}$   $157.74 \mu\text{m}$  line ([C II]  $158 \mu\text{m}$ ) emission—the latter being one of the prime coolants of the cold interstellar medium (ISM; Wolfire et al. 2022)—toward optically luminous quasars ( $M_{1450} \lesssim -26$  mag) by the Atacama Large Millimeter/submillimeter Array (ALMA) have revealed that vigorous starbursts (star formation rate,  $\text{SFR} \gtrsim 100 - 1000 M_{\odot} \text{yr}^{-1}$ ) and huge amounts of dust ( $\sim 10^8 M_{\odot}$ ) and gas ( $\sim 10^{10} M_{\odot}$ ) are usually associated with these quasars (e.g., Wang et al. 2013; Venemans et al. 2016, 2020; Decarli et al. 2022). Although the prevalence of massive AGN-driven outflows remains unclear from observations of the neutral ISM (Bischetti et al. 2019; Novak et al. 2020; Salak et al. 2024), fast ionized outflows (probed by, e.g., [O III]  $5007 \text{ \AA}$ ) are frequently seen in  $z > 6$  quasars with recent James Webb Space Telescope (JWST) observations (e.g., Marshall et al. 2023; Yang et al. 2023; Yue et al. 2024; Loiacono et al. 2024).

While multiwavelength observations of quasars have progressed significantly in recent years, understanding of their progenitors lags behind. Some limited studies on partially dust-obscured quasars (Fujimoto et al. 2022) and starburst galaxies (Riechers et al. 2013; Marrone et al. 2018; Zavala et al. 2018), both of which may represent earlier evolutionary phases than the UV-bright quasar phase, indeed have revealed very rapid mass assembly in these systems at  $z > 6 - 7$ . Closely interacting galaxies are considered to be an earlier evolutionary stage than these, yet there are very few examples known to host SMBHs at  $z \gtrsim 6$  (Yue et al. 2021, 2023). For example, Neeleman et al. (2019) studied five pairs of quasar host-companion galaxies at [C II] and identified evidence of tidal interaction in three of them. Some other works have also found companion galaxies around quasars at  $z > 5 - 6$  (e.g., Decarli et al. 2017; Venemans et al. 2020). Decarli et al. (2019) performed high-resolution [C II] and FIR continuum observations of another quasar-galaxy pair PJ308-21 at  $z = 6.23$  that hosts an SMBH of  $\sim 3 \times 10^9 M_{\odot}$  (Loiacono et al. 2024), revealing a large amount of cold ISM and the highly interacting nature of the system (two companions with projected distances of  $\sim 5$  and  $\gtrsim 10$  kpc, respectively).

However, the interacting quasars targeted in the above papers are intrinsically as luminous as those of the other, isolated luminous quasars at  $z > 6$  (such as those discovered by the Sloan Digital Sky Survey or SDSS), suggesting that the phase of active galaxy interaction had already happened. On the other hand, hydrodynamic simulations of mergers of galaxies predict that both SFR and quasar luminosity increase by orders of magnitude when gas-rich galaxies merge (e.g., Hopkins et al. 2006). Thus, progenitors in the earlier interaction

phase, which will evolve to the luminous quasars currently observed, are anticipated to be much fainter. Wide-field optical deep imaging surveys, such as the Subaru Hyper Suprime-Cam (HSC) Strategic Survey (Aihara et al. 2018), are useful to search for such faint objects. Indeed, we have established a multiwavelength follow-up consortium for  $z \gtrsim 6$  quasars discovered by the HSC survey, the Subaru High- $z$  Exploration of Low-Luminosity Quasars (e.g., Matsuoka et al. 2016, 2018a, 2018b, 2019, 2022), and so far discovered  $> 150$  low-luminosity quasars down to  $M_{1450} \sim -22$  mag at  $z > 6$ .

### 1.1. Our Target: A Pair of Quasars at $z = 6.05$

This paper presents our ALMA Cycle 7 observations of the [C II]  $158 \mu\text{m}$  line and the underlying rest-frame FIR continuum emission toward the twin quasar system at  $z = 6.05$  discovered by our Subaru HSC survey, namely HSC J121503.42-014858.7 and HSC J121503.55-014859.3 (hereafter, C1 and C2), separated by 12 kpc projected on the sky (Matsuoka et al. 2024). This is the most distant quasar pair (projected separation  $\lesssim 10$  kpc,  $\Delta z \lesssim 0.01$ ) known to date: the discovery and rest-UV properties of these quasars are reported in our companion paper (Matsuoka et al. 2024). The presence of pair quasars is a natural consequence of the hierarchical structure formation, yet the sample is very limited, due to the rarity of SMBHs and the relatively short duration of the AGN phase.

The two quasars in this study have similar rest-UV properties, with  $M_{1450} = -23.11$  mag (C1) and  $M_{1450} = -22.66$  mag (C2): these correspond to quasar bolometric luminosities ( $L_{\text{bol}}$ ) of  $6.2 \times 10^{45} \text{ erg s}^{-1}$  (C1) and  $4.1 \times 10^{45} \text{ erg s}^{-1}$  (C2). The UV magnitudes of these are roughly 10 times higher than the knee of the galaxy luminosity function at  $z \sim 6$  (Harikane et al. 2022), but are fainter than the characteristic value of the  $z \sim 6$  quasar luminosity function ( $M_{1450} = -24.9$  mag; Matsuoka et al. 2018c). The quasar nature of C1 + C2 has been further confirmed by the detections of broad Ly $\alpha$  (FWHM  $> 1000 \text{ km s}^{-1}$ ) in both objects with high luminosities ( $> 10^{43} \text{ erg s}^{-1}$ ). The broad Ly $\alpha$  components are sensitive to  $M_{\text{BH}}$  (Takahashi et al. 2024); Matsuoka et al. (2024) estimated their masses to be  $\log(M_{\text{BH}}/M_{\odot}) \simeq 8.1$  each, corresponding to Eddington ratios of  $\sim 0.4$  (C1) and  $\sim 0.3$  (C2).

Throughout this work, we adopt the concordant Lambda cold dark matter cosmology, with  $H_0 = 70 \text{ km s}^{-1} \text{ Mpc}^{-1}$ ,  $\Omega_M = 0.3$ , and  $\Omega_{\Lambda} = 0.7$ . At the redshift of the source ( $z = 6.05$ ), the age of the Universe is 0.905 Gyr and an angular size of  $1''$  corresponds to a proper distance of 5.68 kpc.

## 2. ALMA Observations

Our observations were conducted as an ALMA Director's Discretionary Time (DDT) program (2019.A.00019.S; PI: T. Izumi). There were two executions in ALMA Band 6 (centered on  $\lambda_{\text{obs}} = 1.1 \text{ mm}$ ) on 2020 February 29, in a  $\sim 23''$  diameter field of view with 41 antennas. Three spectral windows (each  $\sim 1.875 \text{ GHz}$  wide) were placed on one sideband to maximize the contiguous frequency coverage. We set the phase-tracking center of this pointing to  $(\alpha_{\text{ICRS}}, \delta_{\text{ICRS}}) = (12^{\text{h}}15^{\text{m}}03^{\text{s}}.420, -01^{\circ}48'58''70)$ , which corresponds to the optical position of C1. The baseline length ranged from 15.1 m to 783.5 m, resulting in a maximum recoverable scale of  $\sim 5''$ . Two quasars, J1256-0547 and J1217-0029, were observed as a flux/bandpass calibrator and a phase calibrator, respectively. The total on-source time was 106 minutes.

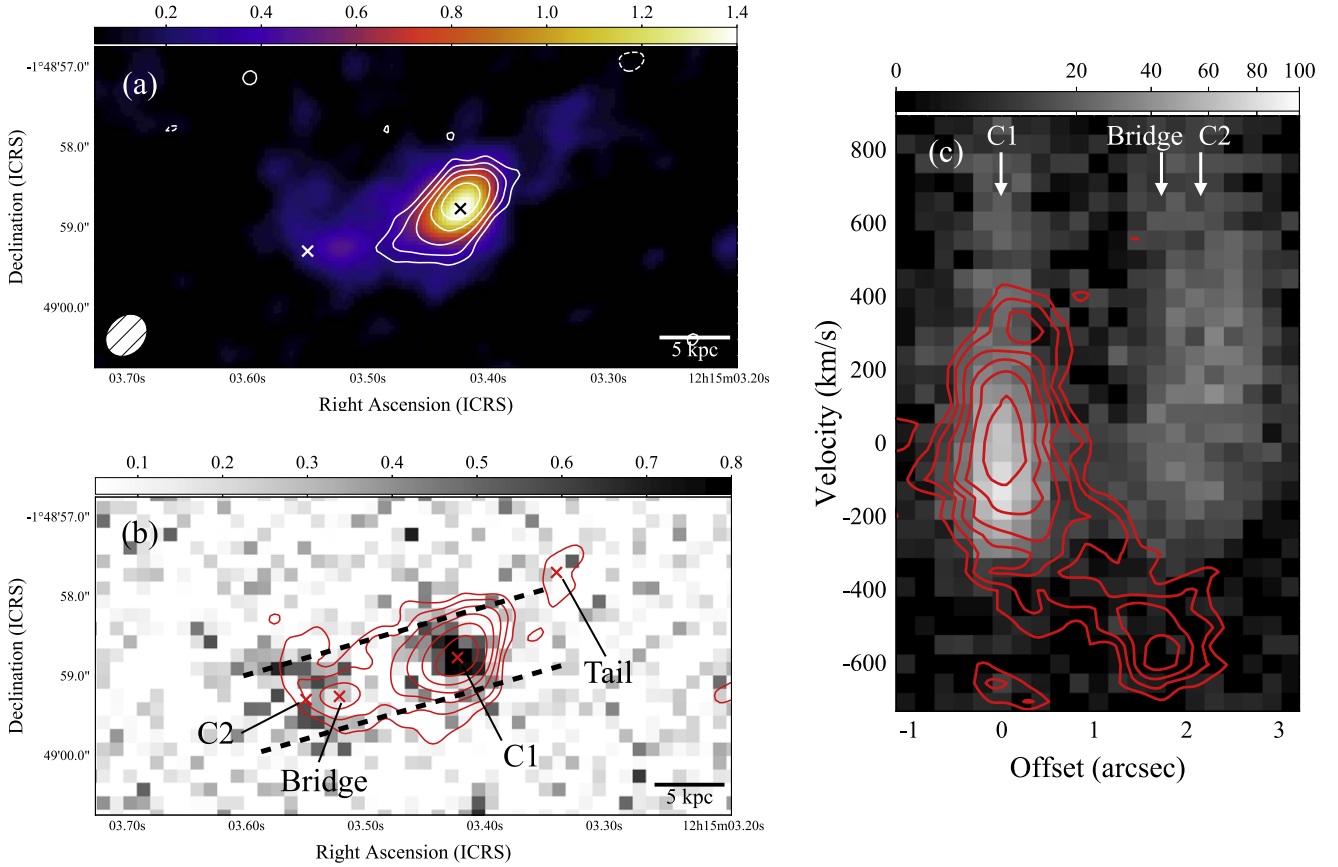


**Figure 1.** (a) Spatial distributions of the velocity-integrated (i.e., moment 0) [C II] (color;  $\text{Jy beam}^{-1} \text{ km s}^{-1}$  unit,  $1\sigma = 0.039 \text{ Jy beam}^{-1} \text{ km s}^{-1}$ ) and the rest-FIR continuum emission (contours) of the pair system. The contours start at  $\pm 3\sigma$  ( $1\sigma = 17.2 \mu\text{Jy beam}^{-1}$ ) and increase by factors of  $\sqrt{2}$ . The crosses mark the locations of C1 and C2 (the latter is determined as the flux-weighted center of the HSC  $z$ -band map (gray scale in arbitrary units)). The contours start at  $\pm 5\sigma$  and increase by factors of  $\sqrt{2}$ . Notable features including C1 and C2 are marked by the crosses. The pseudo-slit used to extract the PVD in panel (c) is also marked (length  $\sim 4''$ , width  $= 1''$ , PA  $= 106^\circ$  measured counterclockwise from north). (c) PVD of Ly $\alpha$  (Matsuoka et al. 2024) in gray scale (arbitrary unit) and that of [C II] in contours (starting from  $2\sigma$  and increasing by factors of  $\sqrt{2}$ ,  $1\sigma = 0.14 \text{ mJy beam}^{-1}$ ). The position of C1 and its [C II] line center velocity are set to the origin of the coordinates. The spatial locations of C1, C2, and the Bridge are marked.

The data were first pipeline-processed using CASA (McMullin et al. 2007; CASA Team et al. 2022) v.5.6 and further analyzed with v.6.1. All images presented in this work were reconstructed using the `tclean` task down to the  $3\sigma$  level, with Briggs weighting (robust = 2.0) to maximize the point-source sensitivity. For the [C II] cube, we averaged several channels to obtain a velocity resolution of  $50 \text{ km s}^{-1}$ , which resulted in a  $1\sigma$  channel sensitivity of  $0.14 \text{ mJy beam}^{-1}$  (beam size  $= 0''.57 \times 0''.46$ , P.A.  $= -41^\circ.2$ ). Line-free channels were integrated to generate a continuum map ( $0''.56 \times 0''.45$ , P.A.  $= -43^\circ.1$ ,  $1\sigma = 17.2 \mu\text{Jy beam}^{-1}$ ), which we subtracted in the  $uv$  plane using the task `uvcontsub` with a first-order polynomial function, before making the line cube. This continuum map was made with the `msf` mode of the `tclean` task. In this paper, we show only statistical errors, unless mentioned otherwise. The absolute flux uncertainty is  $\sim 10\%$  (ALMA Cycle 7 Proposer’s Guide). We also used the MIRIAD software (Sault et al. 1995) for some analyses.

### 3. Results

#### 3.1. A Galaxy Merger Caught in the Act

We detected the [C II] emission from both C1 and C2, and FIR continuum emission mainly from C1, as shown in Figure 1(a). The emission properties as well as relevant physical quantities are

summarized in Table 1. It is noteworthy that the location of C1 (defined from the HSC  $z$ -band map; Figure 1(b)) precisely coincides with the peak position of the [C II] velocity-integrated intensity map, confirming the astrometric accuracy of our observations. However, we found that the location of C2 is offset from the nearest local maximum of the [C II] emission by  $0''.42$  or  $2.4 \text{ kpc}$ . This local maximum lies between C1 and C2, and we refer to it as the “Bridge” hereafter. Note that the location of C2 is determined as the flux-weighted center of the HSC  $z$ -band map. As the  $z$ -band emission is spatially extended, this location does not necessarily correspond to the exact location of the quasar. However, it is evident that the bright  $z$ -band emitting region is offset from this Bridge. We also found significant [C II] emission northwest of C1 (offset by  $\sim 1''.6$  or  $9.3 \text{ kpc}$ ), which we refer to the “Tail” in this work. Both the Bridge and the Tail are most likely formed by interactions of the host galaxies of C1 and C2.

Figure 1(c) compares the position-velocity diagram (PVD) of Ly $\alpha$  (Matsuoka et al. 2024) and that of [C II]. It is also clear from this comparison that C2 (bright in Ly $\alpha$ ) and the Bridge (bright in [C II]) are spatially offset. In addition, it is evident that the [C II] redshift<sup>26</sup> of C2 is blueshifted relative to the Ly $\alpha$  redshift reported in Matsuoka et al. (2024) by  $z_{[\text{C II}]} - z_{\text{Ly}\alpha} = -0.008$  (or

<sup>26</sup> The [C II] redshifts of C1 and C2 have been slightly updated from the values we reported in Matsuoka et al. (2024).

**Table 1**  
Rest-FIR Properties of the Pair System

	C1	C2 + Bridge	Tail
R.A. (ICRS)	12 <sup>h</sup> 15 <sup>m</sup> 03 <sup>s</sup> .423	12 <sup>h</sup> 15 <sup>m</sup> 03 <sup>s</sup> .536	12 <sup>h</sup> 15 <sup>m</sup> 03 <sup>s</sup> .340
Decl. (ICRS)	-01°48′58″.77	-01°48′59″.28	-01°48′57″.70
[C II] Emission			
$z_{[\text{C II}]}$	$6.0561 \pm 0.0002$	$6.0447 \pm 0.0003$	$6.0566 \pm 0.0003$
Velocity offset (km s <sup>-1</sup> )	0	$-481 \pm 13$	$22 \pm 14$
FWHM (km s <sup>-1</sup> )	$594 \pm 20$	$361 \pm 30$	$317 \pm 34$
$S_{[\text{C II}]} \Delta V$ (Jy km s <sup>-1</sup> )	$3.67 \pm 0.19$	$0.91 \pm 0.13$	$0.52 \pm 0.13$
$L_{[\text{C II}]}$ (10 <sup>9</sup> L <sub>⊙</sub> )	$3.50 \pm 0.18$	$0.87 \pm 0.12$	$0.49 \pm 0.12$
SFR <sub>[C II]</sub> (M <sub>⊙</sub> yr <sup>-1</sup> )	$305 \pm 16$	$75 \pm 11$	$43 \pm 11$
$M_{\text{H2}}$ (10 <sup>10</sup> M <sub>⊙</sub> )	~10	~2.6	~1.5
Continuum Emission ( $T_{\text{dust}} = 35$ K, $\beta = 1.6$ , $\kappa_{\lambda} = 0.77(850\mu\text{m}/\lambda)^{\beta} \text{cm}^2 \text{g}^{-1}$ )			
$f_{1.1 \text{ mm}}$ (mJy)	$0.63 \pm 0.05$	<0.09	<0.09
$L_{\text{FIR}}$ (10 <sup>11</sup> L <sub>⊙</sub> )	$4.57 \pm 0.36$	<0.71	<0.71
$L_{\text{TIR}}$ (10 <sup>11</sup> L <sub>⊙</sub> )	$5.99 \pm 0.48$	<0.94	<0.94
$M_{\text{dust}}$ (10 <sup>8</sup> M <sub>⊙</sub> )	$1.58 \pm 0.13$	<0.25	<0.25
SFR <sub>TIR</sub> (M <sub>⊙</sub> yr <sup>-1</sup> )	$89 \pm 7$	<12	<12

**Note.** The coordinates indicate the peak positions of the [C II] emission for C1 and the Tail. For C2, we adopt the flux-weighted centroid of the HSC  $z$ -band map (Matsuoka et al. 2024). This is spatially averaged with the position of the Bridge to define the position of C2 + Bridge. We used 1′′.5 and 1′′.0 diameter apertures to extract the emission properties of C1 and the other components, respectively. Upper limits indicate  $3\sigma$  values. The redshifts were determined from single-Gaussian fittings to the [C II] spectra (see Appendix A), but the line fluxes were based on the integrated intensity map (Figure 1).

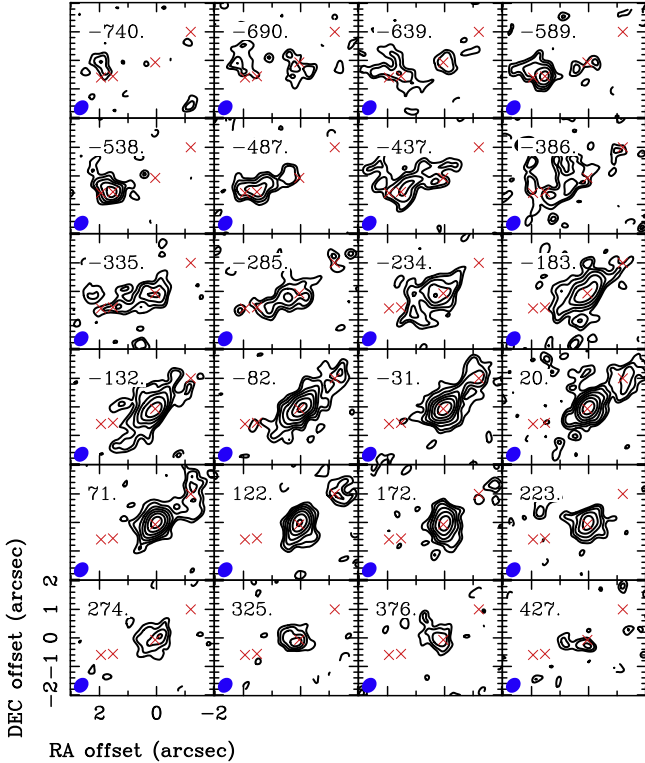


**Figure 2.** Velocity channel maps of the [C II] line emission. Each channel is labeled with its central velocity in kilometers per second relative to the Gaussian centroid of the C1 line profile. The locations of C1 (the origin of the relative coordinates), C2, the Bridge, and the Tail are marked by the crosses in each panel (see also Figure 1). The contours start at  $2\sigma$ , with an increment of  $\sqrt{2}$ , where  $1\sigma = 0.14 \text{ mJy beam}^{-1}$ . The synthesized beam is shown in the bottom left corner of each panel.

$\sim -400 \text{ km s}^{-1}$ ). This velocity offset would be due at least partly to strong Ly $\alpha$  absorption by the intergalactic medium. Indeed, this velocity offset lies nearly at the highest values found in comparably high-redshift galaxies, and those galaxies with high velocity offset tend to show low Ly $\alpha$  escape fractions (Cassata et al. 2020). Another plausible explanation would be that the Bridge is actually the satellite galaxy itself, and its quasar nucleus (C2) is located at the outskirts of this galaxy (host of C1), which may have caused the velocity offset between Ly $\alpha$  and [C II] as well. Future JWST observations of the stellar light distribution will allow us to assess whether this offset is due to a real displacement of the quasar from the gravitational center of the host galaxy.

Figure 2 shows the velocity channel maps of [C II] emission. There is a clear velocity gradient from C2 to the Tail through the Bridge and C1, on scales of  $\sim 4''$  or 23 kpc. This clearly indicates that the pair of galaxies are dynamically coupled. Thus, these galaxies will merge in a short time ( $< 1$  Gyr; e.g., Hopkins et al. 2008) to form a single massive galaxy. In addition to this, we found bright [C II] emission at C1 in multiple channels of  $> 170 \text{ km s}^{-1}$ , suggesting the presence of a dynamically distinct fast component there (see Section 3.4).

### 3.2. Star-forming Nature

With the [C II] line and FIR continuum luminosities, we estimate basic star formation properties of this pair system (Table 1). In order to encompass the emitting region sufficiently, we use a circular aperture of 1′′.5 diameter and 1′′.0 diameter respectively, to measure the fluxes of C1 and the remaining notable regions of C2 + Bridge, and the Tail. Note that as the spatial separation of C2 (12<sup>h</sup>15<sup>m</sup>03<sup>s</sup>.55, -01°48′

59''3) and the Bridge ( $12^{\text{h}}15^{\text{m}}03^{\text{s}}522, -01^{\circ}48'59''26$ ) is only  $0''42$ , we present the value at “C2 + Bridge” by placing the aperture at the middle point ( $12^{\text{h}}15^{\text{m}}03^{\text{s}}536, -01^{\circ}48'59''28$ ) of C2 and the Bridge. The individual [C II] spectra of these regions, as well as the velocity channel maps made with a smoothed  $1''.0$  resolution, are presented in Appendices A and B.

### 3.2.1. From [C II] Emission

Following Solomon & Vanden Bout (2005), the [C II] line luminosity is calculated as

$$L_{[\text{C II}]} / L_{\odot} = 1.04 \times 10^{-3} S_{[\text{C II}]} \Delta V \nu_{\text{rest}} (1+z)^{-1} D_L^2, \quad (1)$$

where  $S_{[\text{C II}]}$  is the [C II] line flux in jansky kilometer per second,  $\nu_{\text{rest}}$  is the rest frequency of 1900.5369 GHz, and  $D_L$  is the luminosity distance to the target. The line luminosities of these regions lie in the range  $(0.5 - 3.5) \times 10^9 L_{\odot}$ . The brightest [C II] emission originates from C1 ( $3.5 \times 10^9 L_{\odot}$ ), which is the highest [C II] luminosity reported for HSC low-luminosity quasars to date that typically have  $L_{[\text{C II}]} < 10^9 L_{\odot}$  (Izumi et al. 2018, 2019, 2021a, 2021b), and is as high as those of optically luminous quasars (e.g., Venemans et al. 2016, 2020; Decarli et al. 2018). This luminosity is also comparable to the luminosities of PJ308–21 (a galaxy merger at  $z = 6.23$ ; Decarli et al. 2019), although C1 ( $M_{1450} = -23.1$  mag) is  $\sim 20$  times fainter than the quasar nucleus of PJ308–21 ( $M_{1450} = -26.3$  mag) at rest-UV wavelength. We speculate that we are witnessing the recent onset of an AGN, which will evolve to a more luminous quasar, in our pair system.

By further assuming that the [C II] line is excited primarily by star formation, we can estimate the SFR using the De Looze et al. (2014) calibration based on local H II/starburst galaxies:  $\log(\text{SFR}_{[\text{C II}]} / M_{\odot} \text{ yr}^{-1}) = -7.06 + 1.0 \times \log(L_{[\text{C II}]} / L_{\odot})$ , with a factor of 2 calibration uncertainty. This relation is applicable to high-redshift ( $z \sim 4 - 8$ ) star-forming galaxies, as demonstrated by Schaerer et al. (2020) and Le Fèvre et al. (2020). With this, we find  $\text{SFR}_{[\text{C II}]} = 305 \pm 16 M_{\odot} \text{ yr}^{-1}$  in C1 and  $75 \pm 11 M_{\odot} \text{ yr}^{-1}$  in C2 + Bridge. If some of the [C II] excitation is due to the quasars, our derived SFRs are upper limits.

The [C II] line luminosity can be used to estimate the molecular gas mass ( $M_{\text{H}_2}$ ) as well (Madden et al. 2020). Using the calibration of Zanella et al. (2018) for a collection of main-sequence and starburst galaxies at intermediate redshifts ( $M_{\text{H}_2} / M_{\odot} \sim 30 \times L_{[\text{C II}]} / L_{\odot}$ ), we find  $M_{\text{H}_2} \sim 10, 2.6, 1.5 \times 10^{10} M_{\odot}$  in the regions of C1, C2 + Bridge, and the Tail, respectively. Note that  $L_{[\text{C II}]}$  has a better correlation with  $M_{\text{H}_2}$  than SFR (Vizgan et al. 2022), which supports the reliability of this line luminosity as a molecular gas-mass tracer and also suggests that the  $L_{[\text{C II}]}$ -SFR relation may arise from the combination of the  $L_{[\text{C II}]}$ - $M_{\text{H}_2}$  relation and the  $M_{\text{H}_2}$ -SFR relation (e.g., Kennicutt & Evans 2012). Hence, the [C II]-based  $M_{\text{H}_2}$  and  $\text{SFR}_{[\text{C II}]}$  reported here are not necessarily independent.

The total [C II] line flux measured with a  $6''.0$  diameter aperture is  $6.6 \text{ Jy km s}^{-1}$ , which translates to  $L_{[\text{C II}]}$ ,  $\text{SFR}_{[\text{C II}]}$ , and  $M_{\text{H}_2}$  of  $6.3 \times 10^9 L_{\odot}$ ,  $550 M_{\odot} \text{ yr}^{-1}$ , and  $1.9 \times 10^{11} M_{\odot}$ , respectively. These values are among the highest ones found in  $z > 6$  quasars of all UV luminosities (e.g., Wang et al. 2010; Venemans et al. 2017; Decarli et al. 2022), demonstrating the presence of active star formation and an immense gaseous

reservoir. Note that Decarli et al. (2022) pointed out discrepancies between [C II]-based  $M_{\text{H}_2}$  and CO-based, [C I]-based, and dust-continuum-based  $M_{\text{H}_2}$ : [C II]-based values are systematically greater than the others by a factor of  $\sim 3 - 5$ . Even so, we claim that the total molecular gas mass of this pair is on the order of  $10^{10} M_{\odot}$ , which is enough to sustain a high SFR (e.g.,  $500 M_{\odot} \text{ yr}^{-1}$ ) and the luminous quasar activity (mass accretion rate  $\sim 10 M_{\odot} \text{ yr}^{-1}$ ) expected to happen after a galaxy merger over  $\sim 10^8 \text{ yr}$ .

### 3.2.2. From FIR Continuum Emission

The rest-FIR continuum emission mainly originates from the regions around C1 Figure 1(a). Our 2D Gaussian fit to the FIR continuum distribution using the CASA task `imfit` found a peak position of (R.A., decl.) = ( $12^{\text{h}}15^{\text{m}}03^{\text{s}}426, -01^{\circ}48'58''73$ ), which agrees well with the optical coordinates of C1 (Matsuoka et al. 2024). The beam-deconvolved size of this 2D Gaussian is  $(1''.19 \pm 0''.14) \times (0''.54 \pm 0''.07)$  or  $(6.76 \text{ kpc} \pm 0.80 \text{ kpc}) \times (3.04 \text{ kpc} \pm 0.40 \text{ kpc})$ , and the peak and area-integrated total flux densities are  $220 \pm 18 \mu\text{Jy beam}^{-1}$  and  $814 \pm 84 \mu\text{Jy}$ , respectively. This high signal-to-noise ratio is well above the threshold of 10 required to make a robust size measurement (Decarli et al. 2018; Venemans et al. 2018). The tidal interaction between the host galaxies would have stretched the star-forming regions, and this intrinsic size is at the extreme of the FIR size distribution of  $z \gtrsim 6$  quasars observed so far (Izumi et al. 2019; Venemans et al. 2020).

From the measured continuum fluxes, we determine the FIR luminosity ( $L_{\text{FIR}}$ ;  $42.5 - 122.5 \mu\text{m}$ ) and the total IR luminosity ( $L_{\text{TIR}}$ ;  $8 - 1000 \mu\text{m}$ ), assuming an optically thin modified blackbody spectrum and values of dust temperature ( $T_{\text{dust}}$ ) and emissivity index  $\beta$ . Note that previous studies on  $z > 6$  luminous quasars with a starburst ( $\text{SFR} \gg 100 M_{\odot} \text{ yr}^{-1}$ ) nature have typically adopted canonical values of  $T_{\text{dust}} = 47 \text{ K}$  and  $\beta = 1.6$ , based on the averaged IR spectral energy distribution of high-redshift optically luminous quasars (Beelen et al. 2006; Leipski et al. 2013). Recent ALMA Band 9 observations toward one of the most luminous quasars at  $z > 6$ , J0100+2802 at  $z = 6.3$ , revealed its  $T_{\text{dust}}$  as 48 K, which is similar to the above value, although its  $\beta$  is as high as 2.6 (Triodi et al. 2023).

However, it seems inappropriate to use such high  $T_{\text{dust}}$  for the galaxies likely in an earlier evolutionary phase, where AGNs and star formation are both much less active than the averaged sample of, for example, Beelen et al. (2006). Hence, for the time being, until we are constrained by multiband observations, we assume  $T_{\text{dust}} = 35 \text{ K}$ , a typical value in local LIRGs (interacting galaxies are usually categorized as LIRGs at  $z \sim 0$ ; e.g., U et al. 2012). This value (35 K) is still within a range of  $T_{\text{dust}}$  observed in  $z \sim 6$  main-sequence (normal) galaxies (Bakx et al. 2021).

We also correct for the contrast and the additional heating effects of the cosmic microwave background radiation (da Cunha et al. 2013) in Table 1. The dust mass is estimated by adopting a rest-frame mass absorption coefficient of  $\kappa_{\lambda} = 0.77(850 \mu\text{m} / \lambda)^{\beta} \text{ cm}^2 \text{ g}^{-1}$  (Dunne et al. 2000). We emphasize that these results are sensitive to the assumed values of  $T_{\text{dust}}$  and  $\beta$ , which are known to be different in different sources (Leipski et al. 2013; Venemans et al. 2018; Liang et al. 2019).<sup>27</sup> The resultant value of  $L_{[\text{C II}]} / L_{\text{FIR}}$ , which

<sup>27</sup> For example, if we adopt  $T_{\text{dust}} = 47 \text{ K}$ , the resultant  $L_{\text{TIR}}$  and SFR will become  $\sim 2.5$  times higher than the values in Table 1.

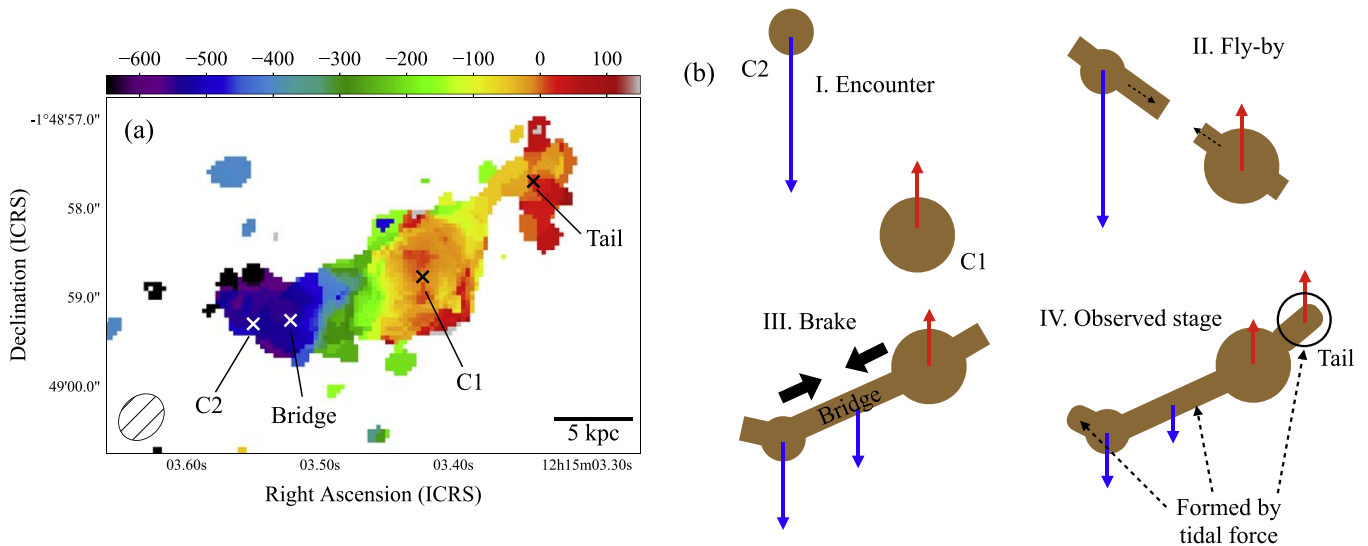


**Figure 3.** (a) Intensity-weighted mean [C II] velocity field map of the pair system. The positions of C1, C2, the Bridge, and the Tail are marked by the crosses (see also Figure 1b). The bottom left ellipse indicates the synthesized beam. The [C II] line center measured at C1, with  $1''.5$  circular aperture (Table 1), is used as the systemic redshift. (b) Schematic explanation of the galaxy–galaxy interaction of the pair system. Four stages (encounter, flyby, brake, and the observed stage) are illustrated.

is sensitive to the physical state of the ISM (e.g., Díaz-Santos et al. 2013; Herrera-Camus et al. 2018), is  $7.7 \times 10^{-3}$ . This is a factor  $\sim 2$  higher than the value for the Milky Way (Carilli & Walter 2013), but still within the range of nearby LIRGs (Díaz-Santos et al. 2013).

By assuming that the total IR continuum emission originates solely from star-forming regions, we estimate the  $\text{SFR}_{\text{TIR}}$  in Table 1 with the conversion  $\text{SFR}_{\text{TIR}} = 1.49 \times 10^{-10} L_{\text{TIR}}/L_{\odot}$  (Murphy et al. 2011). This conversion is based on the Kroupa initial mass function (IMF; Kroupa 2001), but is adjustable for different IMFs, if necessary. Although some works on luminous quasars claim the existence of quasar-heated dust at rest-FIR wavelengths (e.g., Leipski et al. 2014; Izumi et al. 2021a; Tsukui et al. 2023), that effect may not be significant for these low-luminosity quasars. We also found that there is a significant discrepancy between  $\text{SFR}_{[\text{C II}]}$  and  $\text{SFR}_{\text{TIR}}$ , particularly at C2 + Bridge and the Tail. Although one possible explanation is that the actual  $T_{\text{dust}}$  is much higher than the adopted 35 K, it is also plausible that dust-unobscured star formation dominates the total SFR at least at C2 + Bridge and the Tail, and would contribute significantly at C1, as [C II] is sensitive to both obscured and unobscured star formation. Future multiwavelength observations of host-galaxy-scale star formation, such as provided by JWST, will fully characterize the star-forming activity of these host galaxies.

### 3.3. Global Gas Dynamics

Figure 3 shows an intensity-weighted mean [C II] velocity map (moment-1) generated with the CASA task `immoments`, with  $3.5\sigma$  clipping to avoid noisy pixels. As we already saw in the channel maps (Figure 2), there is a clear, global velocity gradient over the system, on scales of  $\sim 4''$ . Similar velocity gradients have also been observed in some quasars on scales of a few kiloparsecs (e.g., Venemans et al. 2016; Decarli et al. 2018; Izumi et al. 2021a), as well as in PJ308–21 (a pair of merging galaxies that hosts a quasar; Decarli et al. 2019).

This global dynamics can be explained by the following steps of tidal disruption of a satellite galaxy (the host galaxy of C2) in close interaction with the heavier host galaxy of C1

(Figure 3b). Note that our attempt here is to explain the global behavior in a qualitative manner, rather than to fit the data with a physical model. We also note that the actual gravitational center of the host galaxy of C2 remains unclear (Section 3.1). Future JWST observations will elucidate the mass distribution of the system and the dynamical nature properly.

- I. Close encounter: two galaxies hosting C1 and C2 start to encounter one another.
- II. Flyby: the galaxies are passing by one another. Gaseous material starts to be expelled from the two galaxies due to tidal interaction, which will eventually form the Bridge structure between them, as well as extended structures at the opposite sides of the galaxies (i.e., the Tail).
- III. Braking phase: this process happens due to the gravitational deceleration and energy dissipation of the two galaxies.
- IV. The observed stage: both the Bridge and the Tail are well developed due to the tidal force between the galaxies.

This situation is very similar to what has been observed in PJ308–21 (Decarli et al. 2019), and this close interaction indicates that the two galaxies will merge into one in a short time.

The actual masses of the host galaxies of C1 and C2, and their ratio, are hard to estimate at this moment, given the highly dynamic nature of the system. Nevertheless, we crudely estimate the dynamical mass ( $M_{\text{dyn}}$ ) of these host galaxies, by following the standard description in studies of  $z > 6$  quasars (e.g., Willott et al. 2015; Venemans et al. 2016; Izumi et al. 2018). Here, the [C II] emission of these galaxies is assumed to be mainly originating from thin rotating disks. The inclination angles ( $i$ ) of the disks are determined from the axis ratios of the beam-deconvolved Gaussian fits to the emitting regions. We use the CASA task `imfit` for this purpose and find the beam-deconvolved major ( $a_{\text{maj}}$ ) and minor ( $a_{\text{min}}$ ) axis sizes as  $a_{\text{maj}} \times a_{\text{min}} = (0''.96 \pm 0''.09) \times (0''.68 \pm 0''.07)$  and  $i = 45^\circ$  for the C1 and  $(0''.85 \pm 0''.26) \times (0''.35 \pm 0''.17)$  and  $i = 66^\circ$  for the C2 + Bridge regions, respectively. Although the latter was measured within a  $1''$  box placed at the midpoint of C2 and the Bridge, we decided to use this to represent the host galaxy of

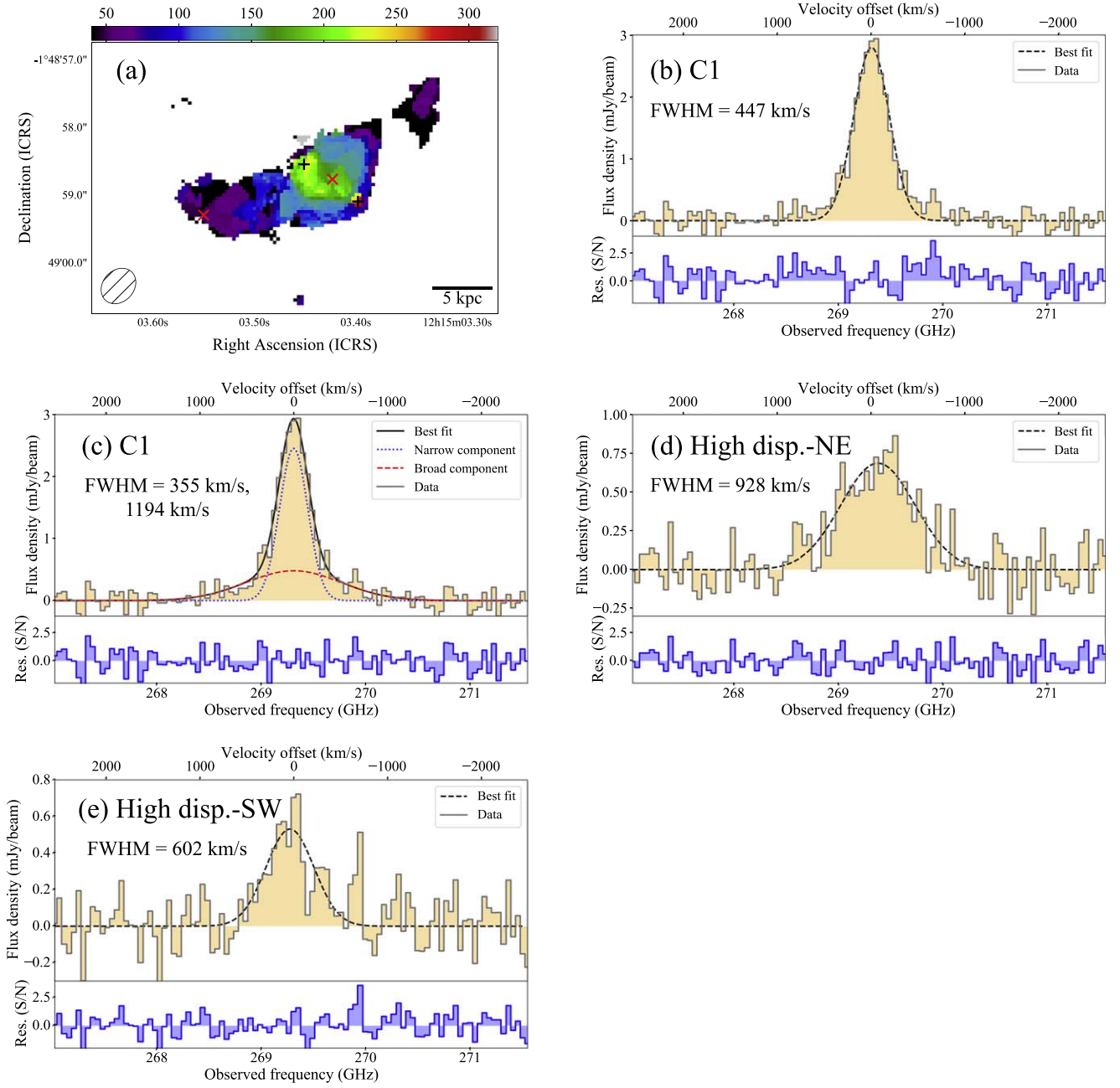


**Figure 4.** (a) Intensity-weighted [C II] velocity dispersion map of the pair system. The two crosses indicate the locations of C1 and C2, whereas the two plus signs indicate the representative location of the high-dispersion regions (NE and SW). (b) The [C II] spectrum measured at C1 with a single-Gaussian fit. (c) The same as (b), but with the result of a double-Gaussian fit. (d) The [C II] spectrum measured at the high-dispersion region NE with a single-Gaussian fit. (e) The same as (d), but for the case of the high-dispersion region SW. In each panel of the line spectrum, residuals after subtracting the model from the data, normalized by the rms value ( $0.14 \text{ mJy beam}^{-1}$ ), together with resultant FWHM of the Gaussian fit, are also shown.

C2, considering the spatial distribution of the [C II] emission around there. The disk size is approximated as  $D = 1.5 \times a_{\text{maj}}$  to account for spatially extended low-level emission, and the circular velocity as  $V_{\text{circ}} = 0.75 \times \text{FWHM}_{[\text{C II}]} / \sin i$ , where  $\text{FWHM}_{[\text{C II}]}$  is the Gaussian FWHM of the [C II] line profile measured on the region ( $594 \text{ km s}^{-1}$  for C1 and  $361 \text{ km s}^{-1}$  for C2 + Bridge). With these, we estimate that  $M_{\text{dyn}} \sim 9 \times 10^{10} M_{\odot}$  for C1 and  $\sim 5 \times 10^{10} M_{\odot}$  for C2, respectively. Given these estimates, we find that their  $M_{\text{dyn}}$  are comparable to  $M_{\text{H}_2}$ , suggesting that this is a major merger system of gas-rich galaxies. The comparable  $M_{\text{BH}}$  of C1 and C2 ( $\sim 10^8 M_{\odot}$ ; Matsuoka et al. 2024) also supports this scenario.

### 3.4. Potential Indication of AGN Feedback

Figure 4(a) shows the intensity-weighted [C II] velocity dispersion map made with the same CASA `immoments` task with  $3.5\sigma$  clipping: if the line profile is purely Gaussian, this dispersion indicates the Gaussian  $\sigma$ . Overall, the dispersion ranges from 50 to  $100 \text{ km s}^{-1}$  over the system, which is comparable to nearby merging galaxies (e.g., Saito et al. 2015; Ciccone et al. 2018). On the other hand, we find globally elevated dispersions around C1 ( $\sim 100 - 150 \text{ km s}^{-1}$ ), as well as linearly distributed high-dispersion regions from northeast to southwest across C1. We specify two representative positions along this line, marked with the plus signs in Figure 4(a), which

are referred to as high-dispersion northeast (NE) and southwest (SW) in the following. As these regions are distributed roughly symmetrically to C1, and the regions of high dispersion are relatively localized, we speculate that this is a hint of two-directional (e.g., biconical) AGN-driven outflows, rather than violent shocks due to the merger of galaxies (Díaz-Santos et al. 2016, 2018; Treister et al. 2020).

We first inspect the [C II] line spectrum of C1 (Figure 4(b)), which was measured with a single synthesized beam. We first fit the spectrum with a single-Gaussian model, which returned (peak amplitude, center, FWHM) =  $(2.8 \pm 0.1 \text{ mJy beam}^{-1}, 269.313 \pm 0.005 \text{ GHz}, 447 \pm 12 \text{ km s}^{-1})$ . It is intriguing that there is excess emission from the single Gaussian up to  $\pm 1000 \text{ km s}^{-1}$ , which is also seen in the high-velocity components in the channel maps (Figure 2). Thus, we next fit the data with a double-Gaussian model (Figure 4(c)) by fixing the centroid of the second Gaussian to that of the first Gaussian, and found that the narrow-core component has (peak amplitude, center, FWHM) =  $(2.5 \pm 0.3 \text{ mJy beam}^{-1}, 269.314 \pm 0.005 \text{ GHz}, 355 \pm 21 \text{ km s}^{-1})$  and the broad-wing component has (peak amplitude, center, FWHM) =  $(0.48 \pm 0.11 \text{ mJy beam}^{-1}, 269.314 \text{ GHz (fixed)}, 1194 \pm 193 \text{ km s}^{-1})$ . The addition of this second broad Gaussian is assessed with the standard  $\chi^2$  value: the single-Gaussian fit returns  $\chi^2/\text{dof} = 85.5/56 = 1.53$ , whereas the double-Gaussian fit returns  $\chi^2/\text{dof} = 42.7/54 = 0.79$  when evaluated over the velocity range of  $\pm 1500 \text{ km s}^{-1}$ . Hence, the double-Gaussian fit is statistically preferred. Furthermore, we find that the line profiles measured at the high-dispersion regions are unusually broad as well (FWHM =  $928 \pm 72 \text{ km s}^{-1}$  at NE,  $602 \pm 75 \text{ km s}^{-1}$  at SW), although they are well fit by a single-Gaussian profile (Figures 4(d) and (e)).

The nearly symmetric appearance of the broad wing at C1 disfavors nearby (unseen) companions as its physical origin: multiple companions at a range of velocity offsets would be required within this single synthesized beam. Hence, we hereafter interpret this broad wing as a potential indication of fast [C II] outflows. We emphasize that such fast neutral outflows (including [C II] and OH 119  $\mu\text{m}$ ) in quasars have been observed in only a few cases at  $z > 6$  (e.g., Izumi et al. 2021a; Salak et al. 2024). Note that, however, further higher-angular-resolution, higher-sensitivity observations are definitely required to confirm the presence of [C II] outflows.

Assuming that the wing has appeared due to outflows, we roughly estimate some basic physical properties. First, the line flux of the broad component at C1 ( $0.61 \pm 0.17 \text{ Jy beam}^{-1} \text{ km s}^{-1}$ ) corresponds to  $L_{[\text{C II}]} = (5.83 \pm 0.16) \times 10^8 L_{\odot}$ . The outflowing atomic mass in neutral hydrogen gas (Hailey-Dunsheath et al. 2010; Ginolfi et al. 2020) is

$$\frac{M_{\text{out}}}{M_{\odot}} = 0.77 \left( \frac{0.7 L_{[\text{C II}], \text{broad}}}{L_{\odot}} \right) \left( \frac{1.4 \times 10^{-4}}{X_{\text{C}^+}} \right) \times \frac{1 + 2e^{-91/T_{\text{ex}}} + n_{\text{crit}}/n}{2e^{-91/T_{\text{ex}}}}, \quad (2)$$

where  $X_{\text{C}^+}$  is the ratio of  $\text{C}^+$  abundance to H,  $T_{\text{ex}}$  is the gas excitation temperature in kelvin,  $n$  is the gas volume density per cubic centimeter, and  $n_{\text{crit}}$  is the critical density of the line ( $\sim 3 \times 10^3 \text{ cm}^{-3}$ ). We assumed that 70% of the [C II] emission originates from neutral photodissociation regions (Hollenbach & Tielens 1997). Following previous studies on [C II] outflows (e.g., Maiolino et al. 2012; Ginolfi et al. 2020; Izumi et al. 2021a), we

estimated  $M_{\text{out}} = (5.6 \pm 1.5) \times 10^8 M_{\odot}$  for  $X_{\text{C}^+} = 1.4 \times 10^{-4}$  and  $T_{\text{ex}} = 200 \text{ K}$ , in the high-density limit ( $n \gg n_{\text{crit}}$ ). As the outflows may smoothly propagate from the quasar outward along the linear regions of high dispersion (Figure 4(a)), here we measure the values within the single synthesized beam placed at C1. This gives the characteristic size (spatial extent) of  $R_{\text{out}} = 1.5 \text{ kpc}$ . Assuming an outflow velocity of  $V_{\text{out}} = \text{FWHM}/2 = 597 \pm 97 \text{ km s}^{-1}$ , which stays constant throughout the flow (Lutz et al. 2020), we obtain a neutral outflow rate of  $\dot{M}_{\text{out, neutral}} = M_{\text{out}} V_{\text{out}} / R_{\text{out}} = 229 \pm 73 M_{\odot} \text{ yr}^{-1}$ . This is comparable to the  $\text{SFR}_{[\text{C II}]}$  measured at C1 (Table 1).

Fluetsch et al. (2019) studied multiphase outflows in nearby star-forming galaxies and AGNs, and found that the total outflow rate  $\dot{M}_{\text{out, total}}$ , including the cold molecular phase, is typically 3 times greater than the atomic-only value. Following this, we speculate that the actual mass-loading factor  $\eta = \dot{M}_{\text{out, total}} / \text{SFR}$  (Veilleux et al. 2020) would be  $\gtrsim 2 - 3$  when we adopt the [C II]-based SFR at C1. This indicates that a significant quenching of star formation is happening, while the gas depletion time is still as long as  $\sim 3 \times 10^8 \text{ yr}$ , as compared to the  $\sim 10^7 \text{ yr}$  scales found in other quasars (e.g., Salak et al. 2024), owing to the rich amount of cold gas in the system.

The driver of this feedback remains unclear, as starburst-driven outflows typically show  $\eta \sim 1 - 3$  (e.g., Ciccone et al. 2014; Gallerani et al. 2018; Ginolfi et al. 2020) and AGN-driven outflows have  $\eta \gtrsim 5$  (e.g., Ciccone et al. 2014; Fiore et al. 2017; Fluetsch et al. 2019): our resultant  $\eta$  is thus intermediate. We note, however, it is rare at any redshift for starburst-driven outflows to reach  $V_{\text{out}} > 500 \text{ km s}^{-1}$  (e.g., Martin 2005; Ginolfi et al. 2020). Supposing the factor of 3 difference from the neutral outflow rate to the total outflow rate, we compute its kinetic energy as  $\sim 2.6 \times 10^{43} \text{ erg s}^{-1}$ . This is only 0.4% of the quasar bolometric luminosity of C1 (Matsuoka et al. 2024), and is much smaller than the value expected in the blast-energy-conserving AGN feedback frequently invoked in coevolution scenarios, even if it exists, to quench the star formation of a host galaxy ( $\sim 5\%$ ; Costa et al. 2014; King & Pounds 2015).

#### 4. Discussion and Summary

We have performed ALMA [C II] line and FIR continuum emission observations toward the  $z = 6.05$  quasar–quasar pair recently discovered by our Subaru/HSC observations (Matsuoka et al. 2024). These quasars are faint at rest-UV ( $M_{1450} \gtrsim -23 \text{ mag}$ ), with modest values of SMBH mass ( $\sim 10^8 M_{\odot}$ ), but we detected very bright [C II] emission, demonstrating that the system is rich in gas. Indeed, we estimated the total  $\text{H}_2$  mass of the system as  $\sim 10^{11} M_{\odot}$  (or at least on the order of  $10^{10} M_{\odot}$ ) from the [C II] luminosity. The masses of the host galaxies, crudely estimated from the [C II] spatial distributions and line widths, are on the same order, showing that the system is very gas-rich. The [C II]-based total SFR of the system is  $\sim 550 M_{\odot} \text{ yr}^{-1}$  (the dust-obscured SFR traced by the IR continuum emission is  $\sim 100 M_{\odot} \text{ yr}^{-1}$ ). The large amount of gas sustains this high star-forming activity, which is most likely triggered by the galaxy–galaxy interaction.

Recent simulations predict an increase in the fraction of SMBH–SMBH pairs with increasing redshift due to higher rates of galaxy–galaxy mergers (e.g., Volonteri et al. 2016, 2022; De Rosa et al. 2019). ALMA observations of  $z \gtrsim 5$  quasars have revealed the presence of companion galaxies (separation  $\lesssim 50 \text{ kpc}$ ) around up to 30%–50% of the systems

(Decarli et al. 2017; Trakhtenbrot et al. 2017; Willott et al. 2017; Neeleman et al. 2019; Nguyen et al. 2020). Recent JWST observations have started to reveal close companion galaxies or mergers in many high- $z$  quasars, which were overlooked in previous works due to insufficient resolutions (e.g., Marshall et al. 2023; Perna et al. 2023). These works demonstrate the importance of mergers of galaxies as the triggering mechanism of luminous quasars at high redshift. These are also in line with the recent hydrodynamic simulations that predict  $z \sim 6$  quasars being a part of complex, gas- and dust-rich merging systems containing multiple sources (Di Mascia et al. 2021; Vito et al. 2022).

However, while some JWST observations have also uncovered dual AGNs (i.e., mergers) in lower-luminosity ( $L_{\text{Bol}} \lesssim 10^{45} \text{ erg s}^{-1}$ ) and lower-BH-mass ( $M_{\text{BH}} \lesssim 10^7 M_{\odot}$ ) populations (e.g., Harikane et al. 2023; Maiolino et al. 2023; Übler et al. 2024), previous works on massive BH pairs with  $M_{\text{BH}} \gtrsim 10^8 M_{\odot}$  were solely performed for luminous quasars with  $M_{1450} \lesssim -26$  mag. Our observations now probe a much lower-luminosity pair of quasars ( $M_{1450} \gtrsim -23$  mag), which can serve as a benchmark of this unexplored regime of low-luminosity, but with a massive BH of  $\sim 10^8 M_{\odot}$ . It is interesting that AGN feedback might be happening already at this early stage (Section 3.4), although its impact on the host galaxy would still be small. Hence, the powerful AGN feedback typically invoked in galaxy evolution models, if it exists, will happen at later evolutionary phases (i.e., the coalescent phase or UV-bright quasar phase).

According to models of merger-driven galaxy evolution (e.g., Sanders et al. 1988; Di Matteo et al. 2005; Hopkins et al. 2006; Lupi et al. 2019), both star formation and AGN are activated by the interaction of gas-rich galaxies. But the activity is further boosted by factors of 10–100 when the actual coalescence/merger happens (Hopkins et al. 2008; Yutani et al. 2022). Thus, we expect that this pair will evolve into a luminous quasar ( $M_{1450} \lesssim -26$  mag) with a high SFR of  $>1000 M_{\odot} \text{ yr}^{-1}$ , comparable to the value for optically luminous (i.e., SDSS-class) quasars observed so far at high redshifts (e.g., Venemans et al. 2018; Bischetti et al. 2021). Such evolution can be sustained by the rich amount of ISM available in this system (Table 1). That is, this pair system may

well correspond to a progenitor of the most luminous quasars in the early Universe. Future multiwavelength observations, including JWST measurements of the stellar mass distribution and ionized outflows (see examples in, e.g., Ding et al. 2023; Marshall et al. 2023), aided with dedicated hydrodynamic simulations, will characterize the nature of this system, and allow us to predict its fate in greater detail.

### Acknowledgments

We appreciate the anonymous reviewer’s very constructive comments for improving this paper. This paper makes use of the following ALMA data: ADS/JAO.ALMA#2019.A.00019. S. ALMA is a partnership of ESO (representing its member states), NSF (USA) and NINS (Japan), together with NRC (Canada), NSTC and ASIAA (Taiwan), and KASI (Republic of Korea), in cooperation with the Republic of Chile. The Joint ALMA Observatory is operated by ESO, AUI/NRAO, and NAOJ. We appreciate the ALMA Director for granting the observing time for the DDT program presented here.

T.I., Y.M., Y.T., M.I., H.U., and K.K. are supported by the Japan Society for the Promotion of Science (JSPS) KAKENHI grant Nos. JP23K03462, JP21H04494, JP23K22537, JP21K03632, [JP20H01953, JP22KK0231, JP23K20240], and [JP17H06130, JP22H04939, JP23K20035], respectively. K.I. acknowledges support under the grant PID2022-136827NB-C44 provided by MCIN/AEI/10.13039/501100011033 / FEDER, UE. T.I. is supported by the ALMA Japan Research Grant for the NAOJ ALMA Project, NAOJ-ALMA-319.

### Appendix A [C II] Line Spectra

The [C II] line spectra measured at the positions of C1, C2, the Bridge, and the Tail (see Figure 1), as well as that of C2 + Bridge, are presented in Figure 5. The results of our single-Gaussian fits to these spectra are summarized in Table 1.

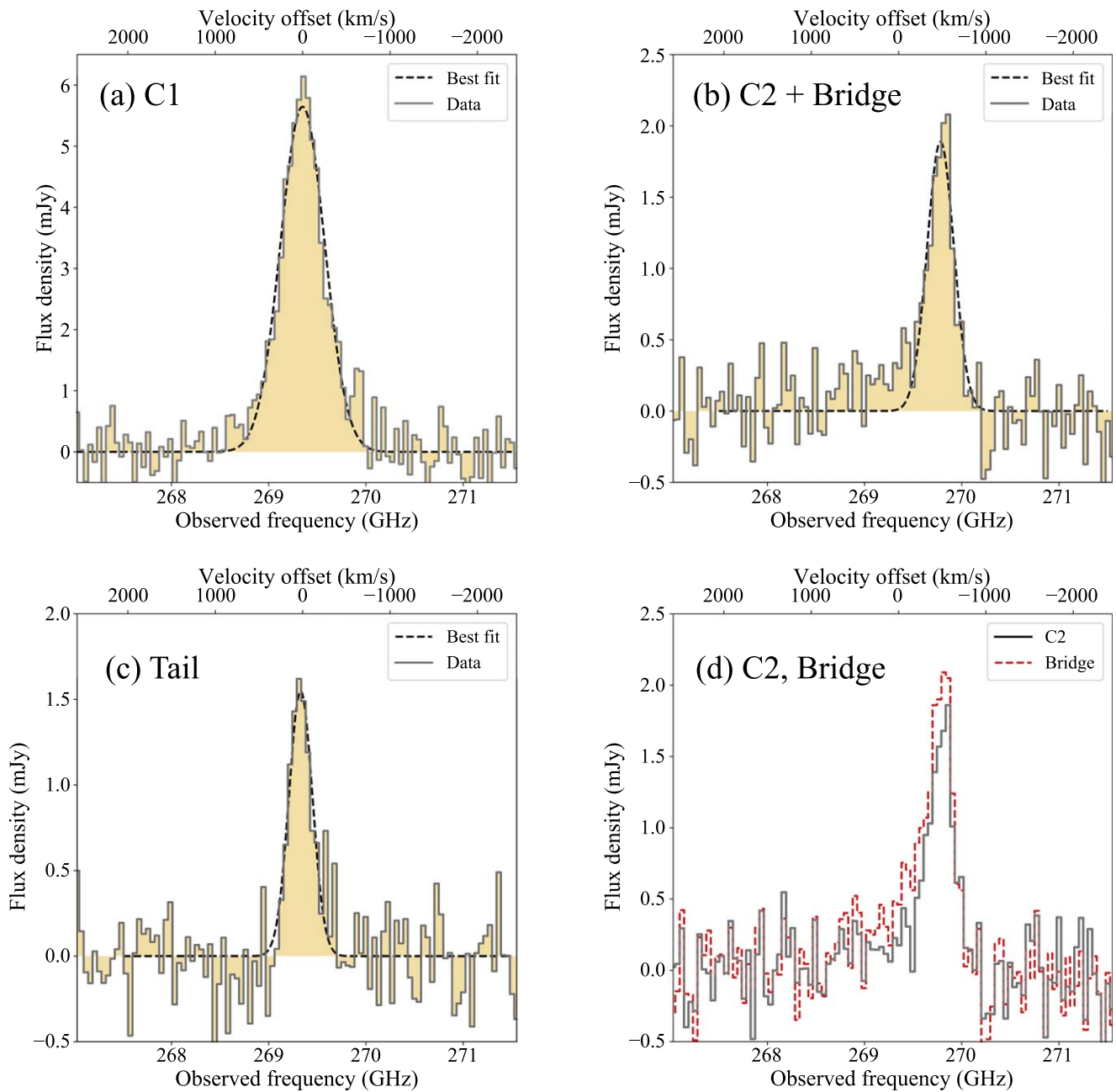


**Figure 5.** (a) [C II] line spectrum measured at the position of C1, with  $1''.5$  aperture. The  $1\sigma$  rms noise level is 0.395 mJy. (b) and (c) [C II] line spectra of C2 + Bridge and the Tail measured with a common  $1''.0$  aperture. The  $1\sigma$  noise level for these spectra is 0.254 mJy. In panels (a), (b), and (c), the results of single-Gaussian fits are also shown (see Table 1 for the results). (d) Individual [C II] spectra of C2 and the Bridge measured with a  $1''.0$  aperture. As the spatial separation between these two positions is small, the measured values here are degenerated.

### Appendix B Smoothed Velocity Channel Maps

We also show the [CII] velocity channel maps measured with a  $1''$  resolution in Figure 6.

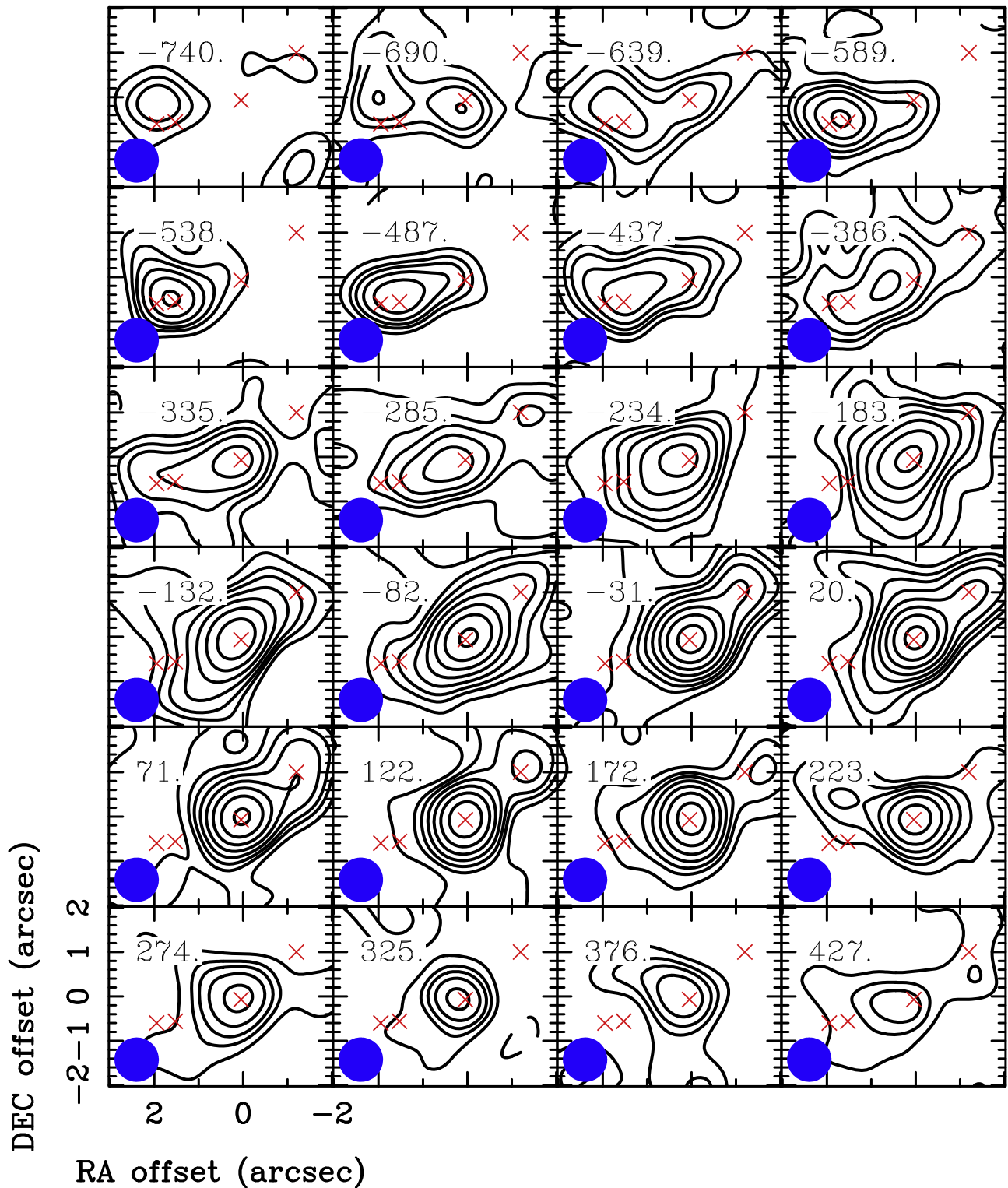


**Figure 6.** Velocity channel maps of the [C II] line of the pair system. The maps are made after smoothing the data to  $1''$  resolution. The first contours indicate  $\pm 1\sigma$  to enhance the faint emission, while the remaining contours are drawn from  $\pm 2\sigma$ , with an increment of  $\sqrt{2}$ , where  $1\sigma = 0.254 \text{ mJy beam}^{-1}$ . The bottom left ellipse in each panel indicates the synthesized beam ( $1''$ ). The four positions (C1, C2, Bridge, and Tail) are also marked (see Figure 1(b)).

## ORCID iDs

Takuma Izumi  <https://orcid.org/0000-0001-9452-0813>  
 Yoshiki Matsuoka  <https://orcid.org/0000-0001-5063-0340>  
 Masafusa Onoue  <https://orcid.org/0000-0003-2984-6803>  
 Michael A. Strauss  <https://orcid.org/0000-0002-0106-7755>  
 Hideki Umehata  <https://orcid.org/0000-0003-1937-0573>  
 John D. Silverman  <https://orcid.org/0000-0002-0000-6977>  
 Tohru Nagao  <https://orcid.org/0000-0002-7402-5441>  
 Masatoshi Imanishi  <https://orcid.org/0000-0001-6186-8792>  
 Kotaro Kohno  <https://orcid.org/0000-0002-4052-2394>  
 Yoshiki Toba  <https://orcid.org/0000-0002-3531-7863>  
 Kazushi Iwasawa  <https://orcid.org/0000-0002-4923-3281>  
 Kouichiro Nakanishi  <https://orcid.org/0000-0002-6939-0372>  
 Mahoshi Sawamura  <https://orcid.org/0009-0003-5438-8303>  
 Seiji Fujimoto  <https://orcid.org/0000-0001-7201-5066>  
 Satoshi Kikuta  <https://orcid.org/0000-0003-3214-9128>  
 Toshihiro Kawaguchi  <https://orcid.org/0000-0002-3866-9645>  
 Kentaro Aoki  <https://orcid.org/0000-0003-4569-1098>  
 Tomotsugu Goto  <https://orcid.org/0000-0002-6821-8669>

## References

- Aalto, S., Garcia-Burillo, S., Muller, S., et al. 2012, *A&A*, 537, A44  
 Aihara, H., Armstrong, R., Bickerton, S., et al. 2018, *PASJ*, 70, S8  
 Bakx, T. J. L. C., Sommovigo, L., Carniani, S., et al. 2021, *MNRAS*, 508, L58  
 Bañados, E., Venemans, B. P., Decarli, R., et al. 2016, *ApJS*, 227, 11  
 Beelen, A., Cox, P., Benford, D. J., et al. 2006, *ApJ*, 642, 694  
 Bischetti, M., Feruglio, C., Piconcelli, E., et al. 2021, *A&A*, 645, A33  
 Bischetti, M., Maiolino, R., Carniani, S., et al. 2019, *A&A*, 630, A59  
 Carilli, C. L., & Walter, F. 2013, *ARA&A*, 51, 105  
 Carnall, A. C., McLure, R. J., Dunlop, J. S., et al. 2023, *Natur*, 619, 716  
 CASA Team, Bean, B., Bhatnagar, S., et al. 2022, *PASP*, 134, 114501  
 Cassata, P., Morselli, L., Faisst, A., et al. 2020, *A&A*, 643, A6  
 Cicone, C., Maiolino, R., Sturm, E., et al. 2014, *A&A*, 562, A21  
 Cicone, C., Severgnini, P., Papadopoulos, P. P., et al. 2018, *ApJ*, 863, 143  
 Costa, T., Sijacki, D., & Haehnelt, M. G. 2014, *MNRAS*, 444, 2355  
 da Cunha, E., Groves, B., Walter, F., et al. 2013, *ApJ*, 766, 13  
 De Looze, I., Cormier, D., Lebouteiller, V., et al. 2014, *A&A*, 568, A62  
 De Rosa, A., Vignali, C., Bogdanović, T., et al. 2019, *NewAR*, 86, 101525  
 Decarli, R., Dotti, M., Bañados, E., et al. 2019, *ApJ*, 880, 157  
 Decarli, R., Pensabene, A., Venemans, B., et al. 2022, *A&A*, 662, A60  
 Decarli, R., Walter, F., Venemans, B. P., et al. 2017, *Natur*, 545, 457  
 Decarli, R., Walter, F., Venemans, B. P., et al. 2018, *ApJ*, 854, 97  
 Di Mascia, F., Gallerani, S., Behrens, C., et al. 2021, *MNRAS*, 503, 2349  
 Di Matteo, T., Springel, V., & Hernquist, L. 2005, *Natur*, 433, 604  
 Díaz-Santos, T., Armus, L., Charmandaris, V., et al. 2013, *ApJ*, 774, 68  
 Díaz-Santos, T., Assef, R. J., Blain, A. W., et al. 2016, *ApJL*, 816, L6  
 Díaz-Santos, T., Assef, R. J., Blain, A. W., et al. 2018, *Sci*, 362, 1034  
 Ding, X., Onoue, M., Silverman, J. D., et al. 2023, *Natur*, 621, 51  
 Dunne, L., Eales, S., Edmunds, M., et al. 2000, *MNRAS*, 315, 115  
 Fan, X., Bañados, E., & Simcoe, R. A. 2023, *ARA&A*, 61, 373  
 Fiore, F., Feruglio, C., Shankar, F., et al. 2017, *A&A*, 601, A143  
 Fluetsch, A., Maiolino, R., Carniani, S., et al. 2019, *MNRAS*, 483, 4586  
 Fujimoto, S., Brammer, G. B., Watson, D., et al. 2022, *Natur*, 604, 261  
 Gallerani, S., Pallottini, A., Feruglio, C., et al. 2018, *MNRAS*, 473, 1909  
 Ginolfi, M., Jones, G. C., Béthermin, M., et al. 2020, *A&A*, 633, A90  
 Goulding, A. D., Greene, J. E., Bezanson, R., et al. 2018, *PASJ*, 70, S37  
 Hailey-Dunsheath, S., Nikola, T., Stacey, G. J., et al. 2010, *ApJL*, 714, L162  
 Harikane, Y., Ono, Y., Ouchi, M., et al. 2022, *ApJS*, 259, 20  
 Harikane, Y., Zhang, Y., Nakajima, K., et al. 2023, *ApJ*, 959, 39  
 Herrera-Camus, R., Sturm, E., Graciá-Carpio, J., et al. 2018, *ApJ*, 861, 95  
 Hollenbach, D. J., & Tielens, A. G. G. M. 1997, *ARA&A*, 35, 179  
 Hopkins, P. F., Hernquist, L., Cox, T. J., & Kereš, D. 2008, *ApJS*, 175, 356  
 Hopkins, P. F., Hernquist, L., Cox, T. J., et al. 2006, *ApJS*, 163, 1  
 Inayoshi, K., Visbal, E., & Haiman, Z. 2020, *ARA&A*, 58, 27  
 Izumi, T., Matsuoka, Y., Fujimoto, S., et al. 2021a, *ApJ*, 914, 36  
 Izumi, T., Onoue, M., Matsuoka, Y., et al. 2019, *PASJ*, 71, 111  
 Izumi, T., Onoue, M., Matsuoka, Y., et al. 2021b, *ApJ*, 908, 235  
 Izumi, T., Onoue, M., Shirakata, H., et al. 2018, *PASJ*, 70, 36  
 Jiang, L., McGreer, I. D., Fan, X., et al. 2016, *ApJ*, 833, 222  
 Kennicutt, R. C., & Evans, N. J. 2012, *ARA&A*, 50, 531  
 King, A., & Pounds, K. 2015, *ARA&A*, 53, 115  
 Kormendy, J., & Ho, L. C. 2013, *ARA&A*, 51, 511  
 Koss, M. J., Blecha, L., Bernhard, P., et al. 2018, *Natur*, 563, 214  
 Kroupa, P. 2001, *MNRAS*, 322, 231  
 Le Fèvre, O., Béthermin, M., Faisst, A., et al. 2020, *A&A*, 643, A1  
 Leipski, C., Meisenheimer, K., Walter, F., et al. 2013, *ApJ*, 772, 103  
 Leipski, C., Meisenheimer, K., Walter, F., et al. 2014, *ApJ*, 785, 154  
 Liang, L., Feldmann, R., Kereš, D., et al. 2019, *MNRAS*, 489, 1397  
 Loiacono, F., Decarli, R., Mignoli, M., et al. 2024, *A&A*, 685, A121  
 Lupi, A., Volonteri, M., Decarli, R., et al. 2019, *MNRAS*, 488, 4004  
 Lutz, D., Sturm, E., Janssen, A., et al. 2020, *A&A*, 633, A134  
 Madau, P., & Dickinson, M. 2014, *ARA&A*, 52, 415  
 Madden, S. C., Cormier, D., Honiy, S., et al. 2020, *A&A*, 643, A141  
 Maiolino, R., Gallerani, S., Neri, R., et al. 2012, *MNRAS*, 425, L66  
 Maiolino, R., Scholtz, J., Curtis-Lake, E., et al. 2023, arXiv:2308.01230  
 Marrone, D. P., Spilker, J. S., Hayward, C. C., et al. 2018, *Natur*, 553, 11  
 Marshall, M. A., Perna, M., Willott, C. J., et al. 2023, *A&A*, 678, A191  
 Martin, C. L. 2005, *ApJ*, 621, 227  
 Matsuoka, Y., Iwasawa, K., Onoue, M., et al. 2018a, *ApJS*, 237, 5  
 Matsuoka, Y., Iwasawa, K., Onoue, M., et al. 2019, *ApJ*, 883, 183  
 Matsuoka, Y., Iwasawa, K., Onoue, M., et al. 2022, *ApJS*, 259, 18  
 Matsuoka, Y., Izumi, T., Onoue, M., et al. 2024, *ApJL*, 965, L4  
 Matsuoka, Y., Onoue, M., Kashikawa, N., et al. 2016, *ApJ*, 828, 26  
 Matsuoka, Y., Onoue, M., Kashikawa, N., et al. 2018b, *PASJ*, 70, S35  
 Matsuoka, Y., Strauss, M. A., Kashikawa, N., et al. 2018c, *ApJ*, 869, 150  
 McMullin, J. P., Waters, B., Schiebel, D., Young, W., & Golap, K. 2007, in ASP Conf. Ser. 376, *Astronomical Data Analysis Software and Systems XVI*, ed. R. A. Shaw, F. Hill, & D. J. Bell (San Francisco, CA: ASP), 127  
 Murphy, E. J., Condon, J. J., Schinnerer, E., et al. 2011, *ApJ*, 737, 67  
 Neeleman, M., Bañados, E., Walter, F., et al. 2019, *ApJ*, 882, 10  
 Nesvadba, N. P. H., Lehnert, M. D., De Breuck, C., Gilbert, A. M., & van Breugel, W. 2008, *A&A*, 491, 407  
 Nguyen, N. H., Lira, P., Trakhtenbrot, B., et al. 2020, *ApJ*, 895, 74  
 Novak, M., Venemans, B. P., Walter, F., et al. 2020, *ApJ*, 904, 131  
 Perna, M., Arribas, S., Marshall, M., et al. 2023, *A&A*, 679, A89  
 Riechers, D. A., Bradford, C. M., Clements, D. L., et al. 2013, *Natur*, 496, 329  
 Saito, T., Iono, D., Yun, M. S., et al. 2015, *ApJ*, 803, 60  
 Salak, D., Hashimoto, T., Inoue, A. K., et al. 2024, *ApJ*, 962, 1  
 Sanders, D. B., Soifer, B. T., Elias, J. H., et al. 1988, *ApJ*, 325, 74  
 Schärer, D., Ginolfi, M., Béthermin, M., et al. 2020, *A&A*, 643, A3  
 Sault, R. J., Teuben, P. J., & Wright, M. C. H. 1995, in ASP Conf. Ser. 77, *Astronomical Data Analysis Software and Systems IV*, ed. R. A. Shaw, H. E. Payne, & J. J. E. Hayes (San Francisco, CA: ASP), 433  
 Silverman, J. D., Kampczyk, P., Jahnke, K., et al. 2011, *ApJ*, 743, 2  
 Solomon, P. M., & Vanden Bout, P. A. 2005, *ARA&A*, 43, 677  
 Takahashi, A., Matsuoka, Y., Onoue, M., et al. 2024, *ApJ*, 960, 112  
 Trakhtenbrot, B., Lira, P., Netzer, H., et al. 2017, *ApJ*, 836, 8  
 Treister, E., Messias, H., Privon, G. C., et al. 2020, *ApJ*, 890, 149  
 Tripodi, R., Feruglio, C., Kemper, F., et al. 2023, *ApJL*, 946, L45  
 Tsukui, T., Wisnioski, E., Krumholz, M. R., & Battisti, A. 2023, *MNRAS*, 523, 4654  
 U, V., Sanders, D. B., Mazzarella, J. M., et al. 2012, *ApJS*, 203, 9  
 Übler, H., Maiolino, R., Pérez-González, P. G., et al. 2024, *MNRAS*, 531, 355  
 Valentino, F., Brammer, G., Gould, K. M. L., et al. 2023, *ApJ*, 947, 20  
 Veilleux, S., Maiolino, R., Bolatto, A. D., & Aalto, S. 2020, *A&ARv*, 28, 2  
 Venemans, B. P., Decarli, R., Walter, F., et al. 2018, *ApJ*, 866, 159  
 Venemans, B. P., Walter, F., Decarli, R., et al. 2017, *ApJ*, 845, 154  
 Venemans, B. P., Walter, F., Neeleman, M., et al. 2020, *ApJ*, 904, 130  
 Venemans, B. P., Walter, F., Zschaechner, L., et al. 2016, *ApJ*, 816, 37  
 Vito, F., Di Mascia, F., Gallerani, S., et al. 2022, *MNRAS*, 514, 1672  
 Vizgan, D., Greve, T. R., Olsen, K. P., et al. 2022, *ApJ*, 929, 92  
 Volonteri, M., Dubois, Y., Pichon, C., & Devriendt, J. 2016, *MNRAS*, 460, 2979  
 Volonteri, M., Pfister, H., Beckmann, R., et al. 2022, *MNRAS*, 514, 640  
 Wang, R., Carilli, C. L., Neri, R., et al. 2010, *ApJ*, 714, 699  
 Wang, R., Wagg, J., Carilli, C. L., et al. 2013, *ApJ*, 773, 44  
 Willott, C. J., Bergeron, J., & Omont, A. 2015, *ApJ*, 801, 123  
 Willott, C. J., Bergeron, J., & Omont, A. 2017, *ApJ*, 850, 108  
 Wolfire, M. G., Vallini, L., & Chevance, M. 2022, *ARA&A*, 60, 247  
 Yang, J., Wang, F., Fan, X., et al. 2023, *ApJL*, 951, L5  
 Yue, M., Eilers, A.-C., Simcoe, R. A., et al. 2024, *ApJ*, 966, 176  
 Yue, M., Fan, X., Yang, J., & Wang, F. 2021, *ApJL*, 921, L27  
 Yue, M., Fan, X., Yang, J., & Wang, F. 2023, *AJ*, 165, 191  
 Yutani, N., Toba, Y., Baba, S., & Wada, K. 2022, *ApJ*, 936, 118  
 Zanella, A., Daddi, E., Magdis, G., et al. 2018, *MNRAS*, 481, 1976  
 Zavala, J. A., Montaña, A., Hughes, D. H., et al. 2018, *NatAs*, 2, 56